Scattering techniques to probe the templating effect in the synthesis of copper hexacyanoferrate nanoparticles via reverse microemulsions

Clémentine Mansas, Cyrielle Rey, Xavier Deschanels, Jérémy Causse

Scattering techniques to probe the templating effect in the synthesis of copper hexacyanoferrate nanoparticles via reverse microemulsions

Clémentine Mansas[#], Cyrielle Rey[#], Xavier Deschanels[#] and Jérémy Causse[#]

[#]ICSM, Univ. Montpellier, CEA, CNRS, ENSCM, Bagnols-sur-Cèze, France.

Abstract

The formation of nanoparticles (NPs) by means of reverse microemulsions results in generally homogeneous shapes with fairly narrow size distributions. We report here a study of the behaviour of the microemulsion (NaAOT/Isooctane/water) during the formation of copper hexacyanoferrate NPs inside water nanodroplets (CuPBA for Prussian Blue Analogous). Small angle X-ray and neutron scattering (SAXS, SANS) provides additional information on the size, shape and interaction between the inverted micelles. SAXS shows that as soon as CuPBA NPs are present in the system, long-range interactions occur between the micelles, even for the smallest amount of NPs. On the other hand, the SANS matching technique allows to consider only the diffusion of the NPs by deactivating the diffusion of the rest of the system. The size of the NPs found with SANS is in agreement with TEM observations for intermediate contents of aqueous phase in the microemulsion (5.1±0.9nm for w=10). Finally, FTIR and XRD confirm the formation of CuPBA networks. Moreover, TEM shows that the size of the NPs is in agreement with the radius of the nanodroplets given by SAXS, except for a higher water content where the system is closer to destabilisation, thus producing larger NPs with a wide size distribution (13.6±4.6nm for w=20) compared to the droplet radius.

1 INTRODUCTION

The family of Prussian blue analogues (PBAs) has been widely studied in recent years because of the wide variety of products it offers by simply modifying the Fe atom with other metal atoms such as Cu, Ni, Zn, Mo, Mn in the famous Prussian blue $KFe^{(III)}Fe^{(II)}(CN)_6$. Thanks to this amazing adaptability, many compounds have been created and tested in various applications. These materials can have interesting optical [1,2], magnetic [3–6] and storage properties [7] and can be used in decontamination of water [8–10], in battery [11–15] and in storage system [16–18]. For example, the nuclear industry generates large quantities of contaminated water and their treatment must be carried out. Prussian blue analogous and more particularly metal hexacyanoferrate NPs represent a valid solution for removing radioactive elements and more particularly Cs [19–21]. For example, silica monolith functionalised with copper hexacyanoferrate nanoparticles were tested[22–25]. Several methods can be used to

synthesise these nanoparticles. It is possible to distinguish between bulk synthesis [20,22,26] and routes using a microemulsion as a template[27–31]. Reverse microemulsions consist in stable dispersion of aqueous droplets in oil phase (W/O). The quantity of solubilized water in the system is defined thanks to w=[water]/[surfactant], the ratio of water to surfactant. A lot of surfactants, anionic (NaAOT, Aerosol OT, sodium bis(2-ethylhexyl)sulfosuccinate)[27,28,31], cationic (CTAB, CetylTrimethylAmmonium Bromide))[32] or non-ionic (Igepal, Triton X 100, Brij)[33–35], can be used in reverse microemulsions. In these cases, surfactant should present hydrophilic/lipophilic balance (HLB) tilted towards hydrophobic side in order to be solubilised in large amounts in organic solvent. Among these surfactants, commercial NaAOT and its modified derivatives have been extensively studied over the last decades. Numerous studies concerning the structure of the microemulsion have been carried out using different techniques: X-ray[36,37], neutron[38,39] and light scattering[40], and also fluorescence[41] and acoustic[42] techniques. These studies suggest the presence of monodisperse spherical reverse micelles [43,44]. A theoretical model can be used to study the system and the work of Pileni et al. provides interesting tools such as a linear equation that allows the droplet radius to be determined as a function of w, (R=0.526+0.150*w)[36,44,45]. Reverse microemulsions are commonly used to synthesise inorganic NPs such as metal[46,47], metal oxide[48–50] and quantum dots[51,52] and allow numerous structures like core-shell[53], multi core-shell[54], and yolk/shell[55] NPs [33]. Nanodroplets of water are used as a reactor for the synthesis of nano-objects, which allows control of particle size and morphology. However, the mechanisms of nanoparticle formation in water droplets are not yet well understood. In most cases, the size of the NPs produced is close to the size of micelles, i.e. a few nanometers. It is true for Cu, CuO[44,56] or iron oxide and CeO_2[35] when w is quite low. For high w, gelatin is often used in order to limit aggregation and sedimentation of the particles because of the microemulsions turn to

emulsions in these conditions[29,56]. However, working with high w is a way to increase particles size keeping a valid template effect.

Finally, there are also examples in the literature of a real templating effect with NPs sizes larger than the reverse micelle size while w is kept at low values. This is particularly true for the synthesis performed with NaAOT where the sodium counterion was exchanged with a metal cation to produce NPs. This method was not only used for PBA NPs, but also for $BaCrO_4$[57]. These studies were mainly achieved by Mann's group[27,28,31]. Vaucher et al. present the modification of the initial NaAOT surfactant, by exchanging Na+ with Co2+, to obtain CoAOT. The modified surfactant is then used to make a microemulsion, allowing the Co ion from the surfactant to react with the precursor $K_4Fe(CN)_6$, present in the water nanodroplets, to form the cobalt hexacyanoferrate $K_2CoFe(CN)_6$, or Co-PBA. At relatively low w's, i.e. 10 and 30, the NPs are monodisperse with sizes of 17nm and 22nm respectively. It is thus proven that the template effect is real while the water nanodroplets are clearly smaller than the NPs, with a diameter of 11nm at w=30. No droplet size was given for w=10 but it is reasonable to assume that it was even smaller than for w=30. In these systems, it is remarkable that the long range templating effect is also observed for long reaction times. These superlattice structures suggest long-range inter-particle interactions in the reverse microemulsion. They are visible for the synthesis of PBA NPs in NaAOT inverse microemulsions. But they are even more impressive in the case of the synthesis of BaCrO4 NPs. Li et al observed uniform platelet NPs 16nm long and 6nm wide stacked in 1D aggregates. While these platelets grow in the microemulsion, a precipitated phase of rectangular superlattices of square BaCrO4 NPs is also observed. The authors argue that the 1D structures represent the initial stages of chain assembly, suggesting that BaCrO4 growth occurs in association with and at the same time as the self-organisation of the micellar aggregate. They explain that one hypothesis is that the linear arrays self-assemble in the

reverse microemulsion through the arrangement between the hydrophobic BaAOT tails. Therefore, the emergence of superlattices in such reverse microemulsion systems, prepared with modified BaAOT, suggests that specific interactions take place between the swollen micelles, even at low w values.

The aim of the present study is to understand how the formation of hexacyanoferrate nanoparticles, and more specifically copper hexacyanoferrate, modifies a template W/O microemulsion. Secondly, the morphology and size of the nanoparticles are also studied.

2 MATERIALS AND METHODS

2.1 Synthesis of the CuPBA nanoparticles

2.1.1 Microemulsion NaAOT (system A)

Microemulsion A is prepared with [NaAOT]=0.1M in isooctane. Small amounts of deionised water are added to produce a reference microemulsion called A-H2O-w with w defined as follows, w=[water]/[NaAOT]. This reference microemulsion is compared to others prepared in the presence of ions in the water droplets in order to assess the role of these charged species. For example, small amounts of a $[K_4Fe(CN)_6]$=0.05M solution are added to produce a microemulsion with the generic name A-Fe-w. The description of the different samples is summarised in Table 1.

2.1.2 Microemulsion CuAOT (system B)

In this case, the surfactant NaAOT is modified to form CuAOT according to the publication of J.Eastoe [58].

The microemulsion B-H_2O-w is prepared with [CuAOT]=0.044M in isooctane with small quantities of water according to w=5, 10 and 20 (Table 1), with w defined as follows w(B-H2O)=[water]/[CuAOT]

2.1.3 Synthesis of CuPBA nanoparticles (system C)

The synthesis of CuPBA NPs is achieved by mixing the microemulsion A-Fe-w and B-H2O-w to form the microemulsion C-CuPBA-w. Now, if A-H2O-w is mixed with B-H2O-w, a microemulsion without NPs is produced, called C-H2O-w. The amount of water in the system can change depending on w, which is between 5 and 20. Microemulsions A and B are only mixed considering the same values of w in order not to mix two systems with different water phase droplet sizes. The volume of microemulsion B-H2O-w added to microemulsion A-Fe-w is adjusted according to n(Cu)/n(Fe)=4/3. The different additions are carried out under ultrasonic stirring. The microemulsions can then be broken to recover the Cu-PBA NPs by adding the same volume of ethanol to the C-CuPBA microemulsion and half as much DMSO. Several cycles of centrifugation (4500 rpm, 20 min) and ethanol washing are performed to recover the NPs. The description of the different samples is summarised in Table 1.

Table 1: Description and name of the different SAXS samples.

SAXS Experiments					
	System A		System B	System C	
Surfactant	[NaAOT]=0.1M		[CuAOT]=0.044M	NaAOT+CuAOT	
Aqueous phase	water	$[K_4Fe(CN)_6]$= 0.05M	water	water	[CuPBA]=0.05M
w	5, 10, 20	5, 10, 20	5, 10, 20	5, 10, 20	5, 10, 20
Oil	isooctane	isooctane	isooctane	isooctane	isooctane
Name	A-H_2O-w	A-Fe-w	B-H_2O-w	C-H_2O-w	C-CuPBA-w

2.2 Small Angle X-ray Scattering (SAXS) experiments

SAXS analyses were performed both in-house at ICSM and at the SWING beamline in Soleil Synchrotron. ICSM experiments were realised in transmission using a molybdenum source

with λ=0.71Å (E=17.45 keV). Monochromatism is obtained using the Xenocs Fox2D mirror. The beam of 0.8 mm is collimated with two slots. Beam intensities were collected on the plate detector MAR345 2D with the detection of the wave vector q between 0.3 and 10 nm^{-1}. Samples were analysed in 2 mm diameter glass capillaries.

Experiments performed in Soleil Synchrotron (SWING), were realised with a 12keV X-ray energy. The distance detector-sample d is equal to 2 m for wide angles and 6 m for small angles. Samples were studied in fixed capillary (Ø=1.5 mm) washed with ethanol between each measurement. Exposure time was set between 250 and 750 ms depending on the scattering intensity of the samples.

Core-shell model (theoretical method)

SAXS results were treated using a core-shell model established with the software SASfit 0.94.2. The total scattering function is given by the combination of two scattering functions, the form factor P(q) and the structure factor S(q) with n the particle number density:

$$I(q) = nP(q)S(q)$$

The model is based on a simple geometric description of the spherical water droplets with a radius, R, dispersed in organic phase with a monolayer of NaAOT (or CuAOT) surfactant molecules (Figure 1). The centre of the micelle, made of water, represents the core of geometric model and the water bounded to the surfactant polar head represents the shell of the model.

The equation related to the core-shell model, the form factor, is:

$$I_{shell}(q, R, d, \Delta\rho_1, \Delta\rho_2) = [K(q, R + d, \Delta\rho_2) - K(q, R, \Delta\rho_2 - \Delta\rho_1)]^2$$

With:

$$K(q,r,\Delta\rho) = \frac{4}{3}\pi r^3 \Delta\rho \, 3\frac{\sin qr - qr\cos qr}{(qr)^3}$$

And $\Delta p_1 = p_1 - p_{oil}$

$\Delta p_2 = p_2 - p_{oil}$

Figure 1 : Schema of a core-shell swollen reverse micelle. ρ_1, ρ_2 and ρ_{OIL}, represent respectively the electronic scattering density of the water core, of the shell (surfactant polar head and water) and of isooctane (oil).

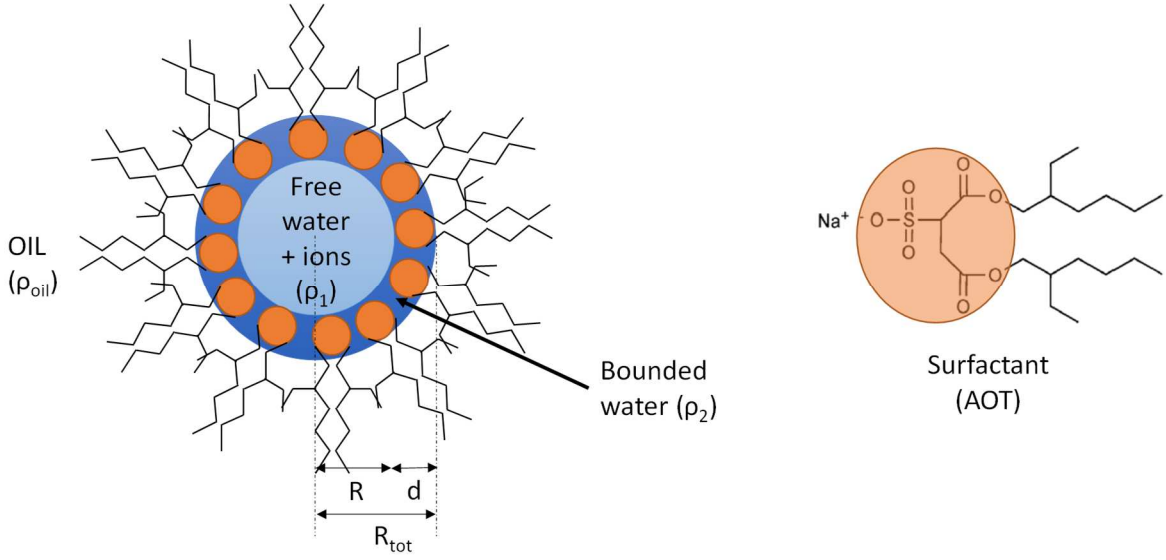

The centre of the micelle is made of free water giving an electronic scattering density contrast between micelle core and oil (isooctane) equals to $\Delta\rho_1$=3.04 10^{10} cm^{-2}. With the addition of PBA nanoparticles, the contrast only slightly differs ($\Delta\rho_1$'=3.10 10^{10} cm^{-2}) because of the weak concentration of PBA. This is the reason why the contrast $\Delta\rho_1$ is used in all calculations. The electronic scattering density contrast $\Delta\rho_2$ of the shell (i.e. water bonded with the polar head of the surfactant) with organic phase (i.e. isooctane) equals to $\Delta\rho_2$=4.39 10^{10} cm^{-2}. The thickness of the polar head groups is estimated around 0.5 nm [59] and the thickness of the water bond is between 0.3 and 0.5 nm[45] so the shell (d) would be between 0.8 and 1 nm while the length of the hydrocarbon chains is approximately equal to 1.2 nm.

The SAXS curves were fitted thanks to the core-shell model defined above with a LogNormal distribution of the micelles radius (ESI). In some cases, a structure factor is added with the "Mass Fractal (Exp Cut-Off)" model that includes R_{tot}, the dimension of an individual scattering object; R_{agg} the size of a fractal aggregate and D, the fractal dimension. The equation of this structure factor is:

$$S(q) = 1 + \frac{D}{{R_{tot}}^{D}} \int_0^{\infty} r^{D-3} h(r, R_{agg}) \frac{\sin qr}{qr} r^2 dr$$

With the cut-off function h(r, R_{agg}) defined as follows:

$$h(r, R_{agg}) = exp\left[-\frac{r}{R_{agg}}\right]$$

2.3 Small Angle Neutron Scattering (SANS) samples

Neutron scattering experiments were performed at the Laboratoire Leon Brillouin LLB, in Orphée reactor on PACE beamline. Three configurations were used, a small angle configuration with a distance detector-sample d=5 m and a wavelength λ=12 Å, a medium angle configuration with d=3 m and λ=5 Å and finally a wide angle configuration with d=1 m and λ=5 Å. Samples were analysed in quartz cells with a thickness of 1 or 2 mm depending on the hydrogen content in the samples.

Figure 2: Neutronic scattering length density of the different compounds used in each case of contrast (ρ in cm^{-2}).

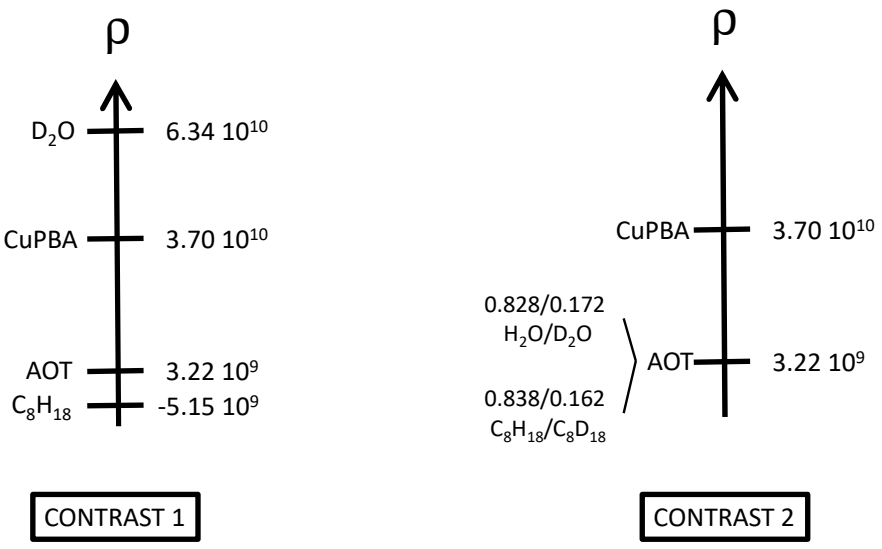

The mix of hydrogenated and deuterated solvents in neutrons experiments allows to adjust the neutronic contrast and to only consider one part of the system. In this paper two different contrasts were studied; contrast 1 and 2 (Figure 2).

The contrast 1 corresponds to classic neutron scattering experiments with deuterated water droplets in isooctane. In this case, the scattering curve is related to the water droplets scattering.

In contrast 2, a mix of H_2O/D_2O with volume ratio (0.828/0.172) and a mix of C_8H_{18}/C_8D_{18} (0.838/0.162) are matching ρ_{AOT}. This means the diffusion length density of the organic and aqueous phase equals NaAOT at 6.22 10^9 cm^{-2}. The contrast is therefore established between CuPBA NPs in the droplets and the rest of the microemulsion (isooctane, water and NaAOT). In these conditions, the scattering curves only depend on the shape and the concentration of the CuPBA NPs.

The synthesis conditions of the CuPBA are changed to be adapted to SANS experiments. The description of the samples dedicated to SANS experiment is presented in Table 2. The concentration of surfactants NaAOT and CuAOT is increased 10 and 30 times keeping the

same w and the same concentration of $K_4Fe(CN)_6$. These modifications were realised to increase the signal to noise ratio so that the scattering level was high enough even when considering micelle extinction, due to the quite low concentration of CuPBA NPs.

Table 2: Description and name of Small Angle Neutrons Scattering samples.

System C	Contrast 1		Contrast 2	
Surfactant	[NaAOT]=0.1, 1 and 3M + [CuAOT]=0.044, 0.44 and 1.32M			
w	5, 10, 20			
Oil phase	C_8H_{18}		C_8H_{18}/C_8D_{18}	
Aqueous phase	D_2O	[CuPBA]= 0.05M	H_2O/D_2O	[CuPBA]= 0.05M
Name	C1-xM-w	C1-xM-CuPBA-w	C2-xM-w	C2-xM-CuPBA-w

For example, considering the name of the samples, C1-0.1M-5 is related to a microemulsion C prepared with NaAOT concentration set at 0.1M without CuPBA NPs in the droplets and with w set at 5 in contrast conditions 1.

2.4 Microscopy

The morphologies of the nanoparticles are studied with transmission electron microscopy (TEM). A drop of the microemulsion containing the nanoparticles is deposited on carbon gold grid. Then grids were dried at 50°C in oven and after washed in ethanol during 20 min. Finally, the grids were dried at room temperature until total evaporation of ethanol. The microscope used was a JEOL 1200EXII (120 kV).

2.5 Analytical methods

The nanoparticles obtained after the elimination of the microemulsion can be analysed thanks to infrared analysis in ATR mode between 4000 and 450 cm^{-1} and X-ray diffraction (XRD). Infrared spectra were performed with the Fourier Transform Infrared Spectroscopy (FTIR) Spectrum 100 from PerkinElmer. Spectra are recorded from 400 to 4000 cm^{-1} with a scanning resolution of 4 cm^{-1}, in ATR mode. The IR spectra were corrected for the background line

thanks to the Spectrum PerkinElmer software. XRD spectra were recorded with a Bruker D8 Advance diffractometer n Bragg-Brentano geometry with Ni-filtered and Cu-Kα radiation, between 2θ=5-80°, step size 0.01° and one second per step.

3 RESULTS

The synthesis of CuPBA NPs in microemulsions is a complex process. Several methods such as X-ray and neutron scattering can be used to determine the size and shape of the droplets in the microemulsion where the nanoparticles are formed. In order to study the formation of CuPBA NPs, a simplified system with just water and no particles is first studied and then the system with particles is analysed.

3.1 Reverse microemulsions

3.1.1 Water droplets without CuPBA

The simplified microemulsion is the mixture of a microemulsion A (NaAOT) and B (CuAOT) with only water inside the droplets. The SAXS results for system A with NaAOT surfactant and three amounts of water (w) are presented in ESI, Figure S1. The curves are fitted using a core-shell model which could be described by a core of water with a surrounding shell made of polar heads of the surfactant and bound water molecules. As w increases, from 5 to 22, the droplet core radius, R, increases from 0.7 to 2.6 nm respectively, according to the equation R=0.112*w+0.056. It is interesting to note that this equation is very close to the one given by Pileni et al R=0.150*w+0.526[44,45]. The slope is of the same order of magnitude, with only one difference concerning the intercept. This difference is mainly due to the model used in the two cases. Indeed, while our study uses a core-shell model with only water in the core, Pileni et al. consider swollen whole micelles. It is therefore expected that the intercept, i.e. the size of the diffusers without water, is closer to 0 in our study. Furthermore, the number of scattering objects decreases as w increases. This is due to the fact that the surfactant

concentration is constant as w increases. These growing objects require more surfactant in each swollen micelle, which leads to a decrease in the number of diffusing objects per unit volume. In fact, as w increases, the water droplets are fewer but larger.

System B is prepared with modified CuAOT, replacing Na with Cu. The inverse microemulsions formed with water in isooctane are different from system A, prepared with conventional NaAOT. Figure S2 shows that for w=5, the SAXS curves show an increasing scattered intensity for low q values. This curve shape is consistent with the observation of Pileni et al. on this type of microemulsion, stating that the water droplets changed from spherical to interconnected cylindrical as w increased[43]. This tends to prove that the droplets are probably aggregated for system B at w=5. Although the microemulsions in system B have aggregated droplets, they remain stable. Mixing of these two microemulsions, A and B, is therefore possible, resulting in system C.

Figure 3: SAXS curves of the microemulsion C with different w (up). Radii of droplets (nm) and number of scattering objects (N) as a function of w.

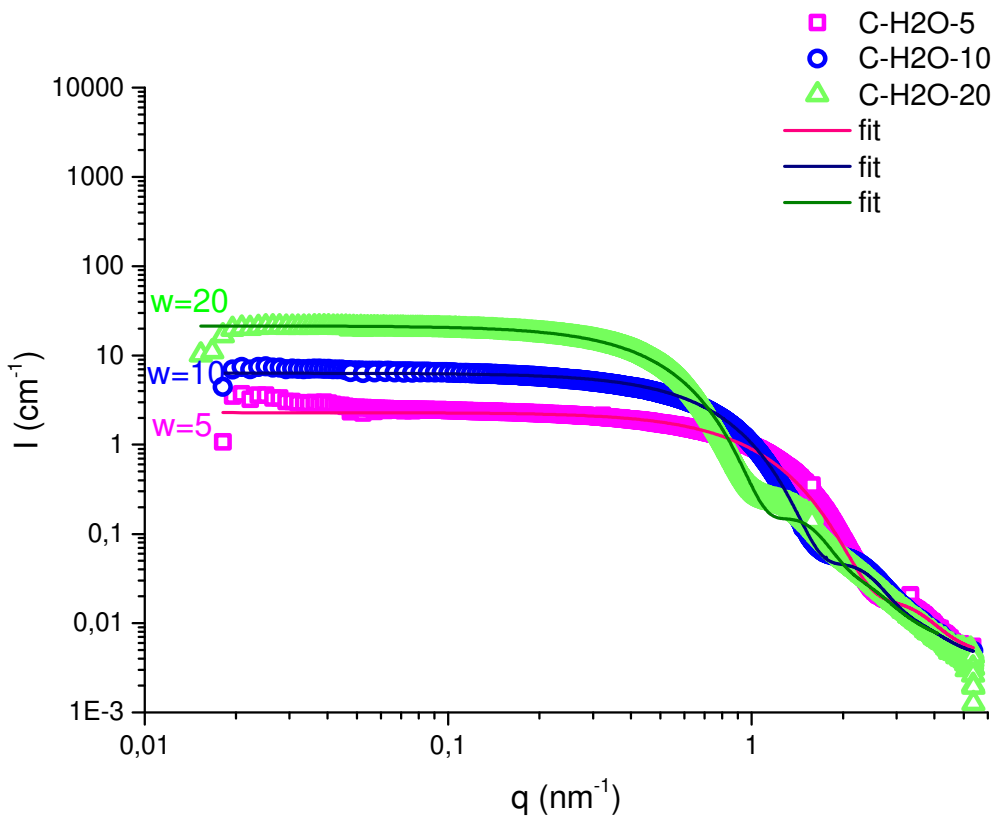

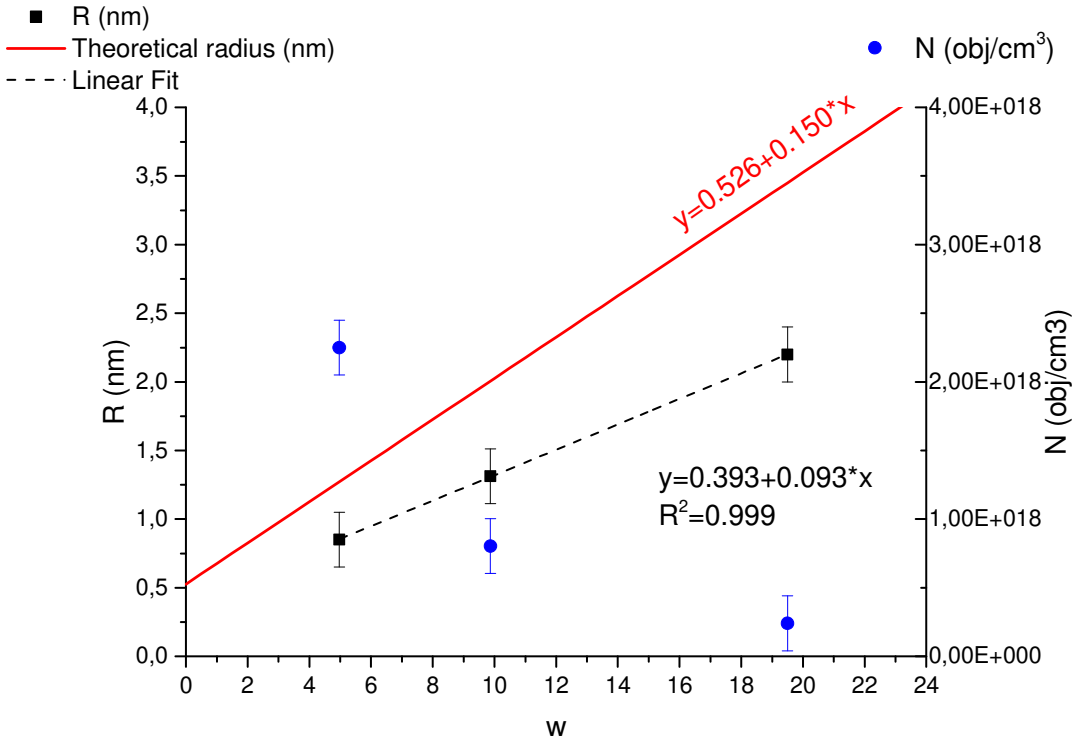

Figure 3 shows the SAXS curves for system C at different w values. These microemulsions are thus the result of mixing microemulsions A (NaAOT) and B (CuAOT) at the same w.

While the dispersed water droplets in systems A and B are different due to the change in the surfactant counterion, system C appears to be quite similar to system A. Indeed, no signs of aggregation or cylindrical shape are observable at low q values of the SAXS curve, and the data set can be fitted with a spherical core-shell model without taking into account any structure factor. The fitting parameters are presented in Table 3.

Table 3: Fit parameters used in Figures 2 and 4.

Samples	w	Form Factor				Contrast		Structure Factor	
		N (ob/cm^3)	R (nm)	d (nm)	R_{tot} (nm)	$\Delta\rho_1$ (cm^{-2})	$\Delta\rho_2$ (cm^{-2})	R_{agg} (nm)	D
C-H_2O-5	5	$2.25\ 10^{18}$	0.9	0.8	1.7	$3.04\ 10^{10}$	$4.39\ 10^{10}$		
C-H_2O-10	10	$8.04\ 10^{17}$	1.3	0.9	2.2	$3.04\ 10^{10}$	$4.39\ 10^{10}$		
C-H_2O-20	20	$2.40\ 10^{17}$	2.2	1.2	3.4	$3.04\ 10^{10}$	$4.39\ 10^{10}$		
C-CuPBA-5	5	$2.25\ 10^{18}$	0.9	0.8	1.7	$3.04\ 10^{10}$	$4.39\ 10^{10}$	30.4	1.9
C-CuPBA-10	10	$8.97\ 10^{17}$	1.3	0.9	2.2	$3.04\ 10^{10}$	$4.39\ 10^{10}$	20.0	2.0
C-CuPBA-20	20	$2.73\ 10^{17}$	2.2	0.9	3.1	$3.04\ 10^{10}$	$4.39\ 10^{10}$	21.0	2.2

After mixing, the water droplets contain both Na and Cu ions. It is interesting to note that the droplet size in system C is smaller than in system A (Fig. 3b; Fig. S1b; Fig. S2b), probably due to the presence of these two ions in the droplets. As w increases in the C microemulsions, from 5 to 20 (Table 3), the droplet radius increases linearly from 0.9 to 2.2 nm according to the equation: R=0.093*w +0.393. This equation is different from the one established for system A with only NaAOT surfactant proving that the mixing of microemulsion A and B led to droplets with lower radii than the simplified system with only NaAOT. Furthermore, the equation found for system C, CuAOT/NaAOT, deviated from the theoretical model, probably due to the introduction of CuAOT, indicating that even though the change of counterion does not change the shape and aggregation of the water droplets in system C, it still has an impact on the droplets. Figure 3 also shows that, as in system A, and for the same reasons, the number of droplets per unit volume decreases as w increases.

Therefore, mixing the two surfactants, NaAOT and CuAOT, tends to create a new microemulsion with smaller droplets than when using NaAOT alone. This decrease in size could be due to the presence of copper ions in the water droplets, which could alter the hydration of the polar groups of the surfactants in the micelles.

3.1.2 Water droplets with CuPBA

3.1.2.1 SAXS results

As seen previously, these microemulsions are studied in order to be used for the synthesis of CuPBA nanoparticles of controlled size. Thus, in this section, the reagent $K_4Fe(CN)_6$ used for the formation of CuPBA is added to the microemulsion A prepared with NaAOT.

First of all, it is important to check how the introduction of $K_4Fe(CN)_6$ changes the microemulsion A. Figure S3 and Table S1 show the SAXS curves and fitting parameters for microemulsion A with and without $K_4Fe(CN)_6$. The major difference between the two systems is visible for small amounts of water at w=5. With the $K_4Fe(CN)_6$ salt, the droplets in

sample A-Fe-5 are smaller than those in sample A-H2O-5 with water. Thus, the addition of a salt induces a decrease in droplet size with a change in the radius of curvature of the micelles, probably due to charge screening of the polar head of the surfactant [36,60]. This conclusion, although less visible, is also valid for the microemulsion at w=10.

Mixing microemulsions A with B therefore produces microemulsions C. If $K_4Fe(CN)_6$ is present in the water droplets of system A, Cu^{2+} ions, which are naturally present in system B due to the presence of the CuAOT surfactant, react with $[Fe(CN)_6]^{4-}$ ions. This reaction precipitates the CuPBA nanoparticles in the water droplets of system C. Figure 4 shows the SAXS curves for the C microemulsions with w increasing from 5 to 20. This figure shows that the C-CuPBA-w systems are very similar to C-H2O-w, with the exception of the increase in diffusion intensity at low q values when CuPBA nanoparticles are present in the microemulsions. The fitting of the curves considers the core-shell model as already mentioned in materials and methods, taking into account the fractal aggregation structure factor, so that the fits describe well the increase at low q values. The fitting parameters are presented in Table 3. They confirm that the drop radius R and the shell thickness d are approximately the same if CuPBA nanoparticles are present in the system. R increases linearly with w according to the equation R=0.093w+0.385. This equation is, not surprisingly, close to that determined for the system without CuPBA (R=0.093w+0.393). Thus, the synthesis of CuPBA NPs only slightly modified the droplet size in the inverse microemulsion while the SAXS curves at low q values presented in Figure 3 may be related to the presence of oversized objects. The increase in scattering intensity appears for quite the same q values regardless of w. It is therefore not surprising that Table 3 shows aggregate sizes of the same order of magnitude of about 20-30 nm. As w increases, the fractal dimension of these oversized objects increases slightly from 1.9 to 2.2 highlighting branched rather than dense aggregates [61]. These oversized domains could be due to the emergence of more water droplet-rich zones,

aggregated under the effect of CuPBA precipitation, which can connect several droplets. Remarkably, these long-range interactions occur even for low values of w, referring to microemulsions known to give small NPs of a few nanometers (Figure 9). These interactions could be related to the superlattices observed by Mann et al.[28]. Indeed, if the formation of superlattice structures is well documented in the dry state when modified CuAOT is used to produce NPs, no additional information is given on the possible modification of the reverse microemulsion itself. In the literature, only disordered NPs have been obtained and no formation of superlattices has been reported with CuPBA unlike CoPBA for example. [27]. However, we believe that this long-range interaction could be a first sign of specific micelle organisation during NP precipitation. Although Mann's group explained the formation of superlattices by the dominance of hydrophobic interactions between the surface adsorbed AOT surfactant and interparticle forces during solvent evaporation from the TEM grid, other authors have given an explanation stemming from a templating effect due to the interaction of water pools.

Figure 4: a) Experimental and fitted SAXS curves of the microemulsions C with CuPBA NPs [CuPBA]=0.05 M for different w. b) Evolution of micelles radius and micelles number density as a function of w.

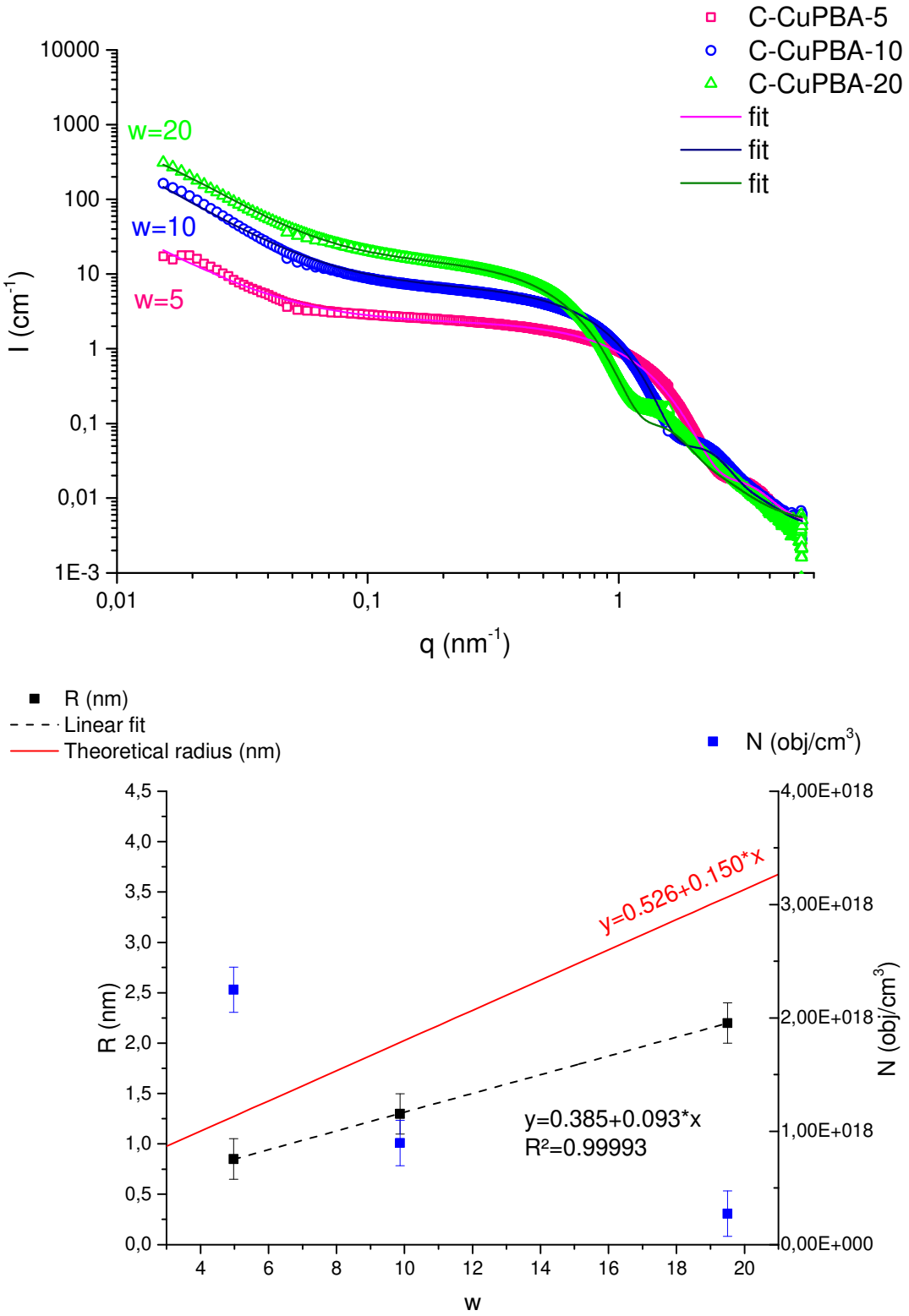

For example, Fortes Martin et al proposed that PEI-coated gold NPs dispersed in water pools of inverted microemulsions modify droplet-droplet interaction resulting in droplet aggregation or fusion. This droplet attraction under the influence of guest NPs has resulted in superlattices[62].

Therefore, the presence of this aggregation structure factor in the SAXS curves could interpret the attractive interactions between the water droplets as a first attempt to explain the initial steps occurring in the liquid phase and leading to an organised network of NPs in the dry state.

3.1.2.2 Probing the inner part of the droplets using SANS matching technique

As already explained in section 2.3, the idea of using SANS is to perform matching technique in order to quench the water droplet diffusion which is dominant in the case of SAXS. Indeed, the quenching of water droplet diffusion highlights the contribution of CuPBA NPs alone. SANS is the only diffusion technique that can probe only the CuPBA NPs inside the droplets in order to evaluate the size of these nanoparticles within the reverse microemulsions. Scattering adjustment is possible using a mixture of deuterated and hydrogenated solvent. Therefore, two different contrast conditions were established, as shown in Figure 2.

Figure 5 shows the SANS diffusion curves for contrast 1 at w=10, with diluted systems in part A and concentrated systems in part B. The latter systems were prepared to maximise the amount of CuPBA without changing its concentration in the water droplets. Thus, the samples annotated 1M and 3M were concentrated by a factor of 10x and 30x respectively compared to the samples presented in part A of Figure 5. It is assumed that increasing the concentration of the surfactant leads to an increase in the number of droplets only without changing the composition of the droplets by keeping constant w and the concentration of CuPBA in the water phase. As expected, SANS curves look like SAXS for diluted systems in Figure 5-a. SANS curves exhibit a Guinier's radius ($I = I_0 e^{-\frac{q^2 R_{Guinier}{}^2}{3}}$) consistent with the radius of the

droplets inner part R obtained by fitting SAXS data in Table 3. Thus, the same conclusions can be drawn: the higher w, the larger the droplets and the introduction of CuPBA NPs does not change the droplet size much. Only one sample, C1-0.1M-CuPBA-20, with a higher w (w=20) shows a strong increase at lower q values, which is a sign of early destabilisation.

The scattering curves of the concentrated samples show a peak in structure due to the increase in water droplet concentration. As observed for the dilute samples, the presence of CuPBA in the droplets does not seem to change the arrangement of the water droplets much (green and blue data sets). The broad peak observed for the 30 times more concentrated samples (3M) is related to a more constrained system where the droplets can no longer move and an equilibrium distance between the centre of the droplets is established. Without Cu PBA in the droplets, the 30 times more concentrated system shows a peak whose position q* corresponds to an equilibrium distance between the droplets of about d*=5.8nm according to the following equation.

$$d^* = \frac{2\pi}{q^*}$$

This distance decreases slightly to 5.4nm in the presence of CuPBA NPs in the droplets confirming that the droplet size is smaller when salts or NPs are present in the aqueous phase, probably due to screening of the interactions between the polar heads of the surfactants. The comparison of R_{tot} (Table 3) with d* supports that these results are consistent as the following equation $d^* \approx 2R_{tot}$ is true for a totally constrained system.

Figure 5: Experimental and fitted SANS curves for the microemulsion C with the contrast 1 a) w=5, 10 and 20 ; [NaAOT]=0.1 M b) concentrated system w=10; [NaAOT]=1 and 3 M.

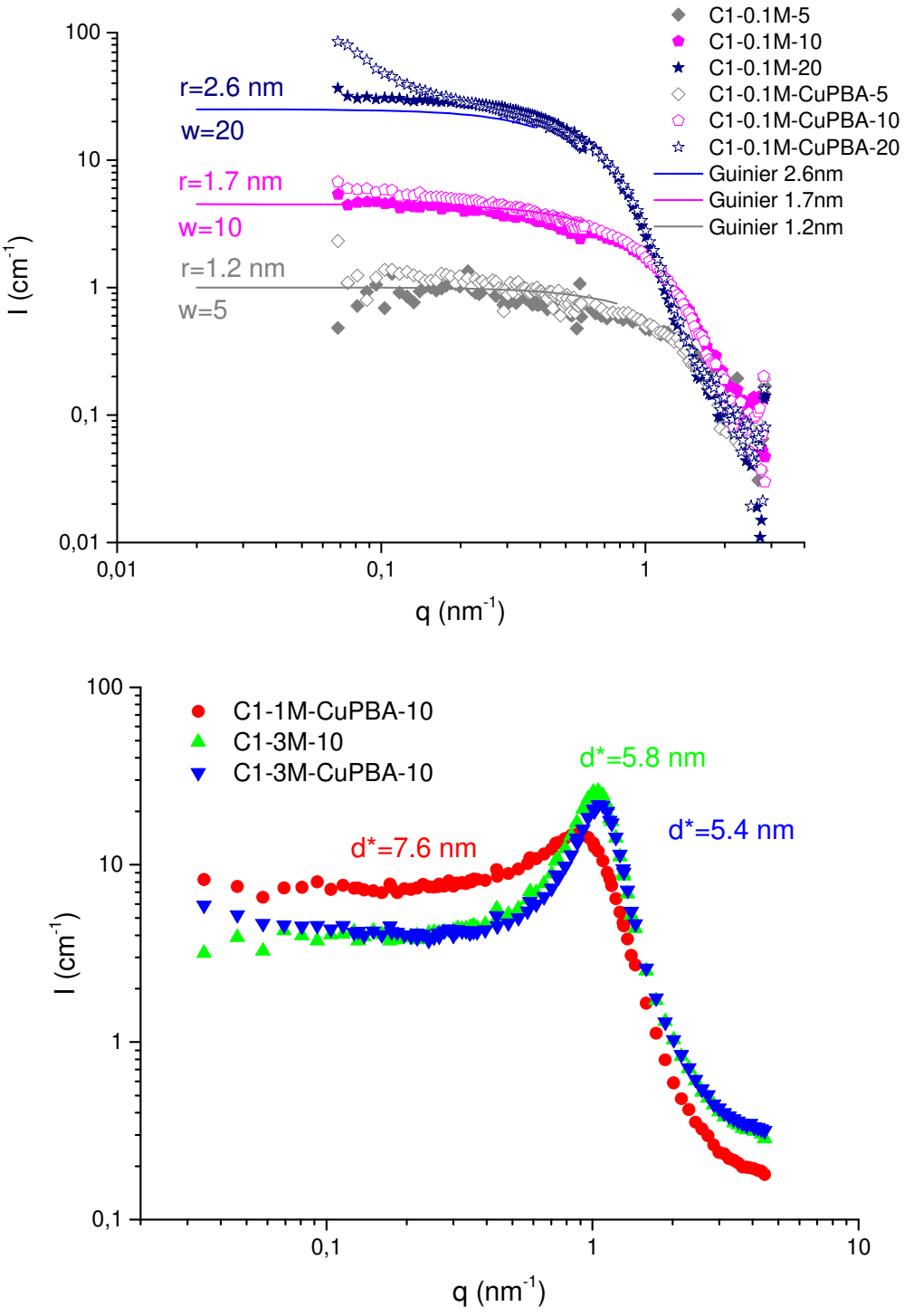

Figure 6 highlights the results for the concentrated microemulsions with contrast 2 promoting droplet diffusion extinction. The purple data series, with a flat curve, is related to the microemulsion without CuPBA NPs in the droplets (C2-3M-10). This curve should be completely flat because all components (aqueous phase, organic phase and surfactant) have the same neutron scattering length density. Thus, no contrast exists between the water droplets, the isooctane and the surfactant and therefore the neutron scattering level is lowered to the maximum. However, a residual peak corresponding to the inter-droplet structure factor is still visible as contrast suppression is quite difficult to achieve when a strong structure peak is present.

Figure 6: Experimental and fitted SAXS curves for microemulsions C2-3M-10 (purple line) and C2-3M-CuPBA-10 (pink line) with the contrast 2 with w=10 and [NaAOT]=3 M.

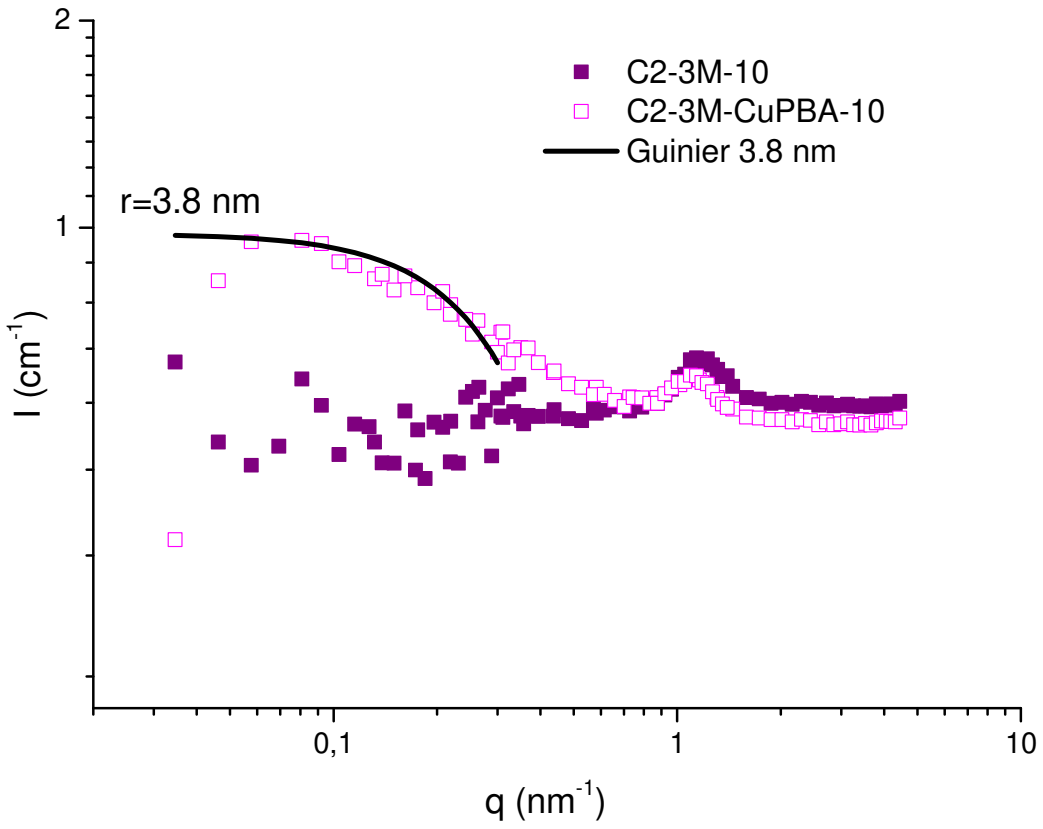

The pink data series corresponds to sample C2-3M-CuPBA-10 with CuPBA nanoparticles. Therefore, the difference between the two curves is directly related to the diffusion of the

NPs. The diffusion intensity is low, of the order of $1cm^{-1}$, justifying the use of a 30 times more concentrated microemulsion. In contrast to the system without CuPBA NPs (purple curve), the scattering intensity is increased at lower q. Using the Guinier approximation, the radius of the scattered object could be estimated at 3.8 nm. This result should be considered with caution due to the statistical weakness of each measurement point. However, it gives a good idea of the order of magnitude of the size of the objects growing in the water droplets. Therefore, the size of the CuPBA NPs is slightly larger but of the same order of magnitude as the droplets whose radius was determined to be 2.7 nm in Figure 5-b for w=10.

3.2 Study of CuPBA nanoparticles

After destabilisation of the microemulsion and recovery of the NPs, chemical and morphological analysis of CuPBA NPs were performed.

FTIR spectrum in Figure 7 highlights the formation of metal hexacyanoferrate materials with the typical C≡N stretching at 2090 cm^{-1} bounded to Fe^{+II} [63]. The stretching vibration of Fe-C bonding at 465 cm^{-1} and the bending vibration of Fe- C≡N around 594 cm^{-1} bounded to Fe^{+II} are also present. The reference spectrum of $K_4Fe(CN)_6$ salt also shows the stretching vibration of the C≡N bound, but for lower wavelengths than CuPBA, at 2040 cm^{-1}. This wavelength shift clearly demonstrates that all the $K_4Fe(CN)_6$ salt present in the water droplets of the microemulsion has reacted with Cu^{2+} moieties to form CuPBA.

Figure 7: Infrared spectra of the samples C-CuPBA-w for different w.

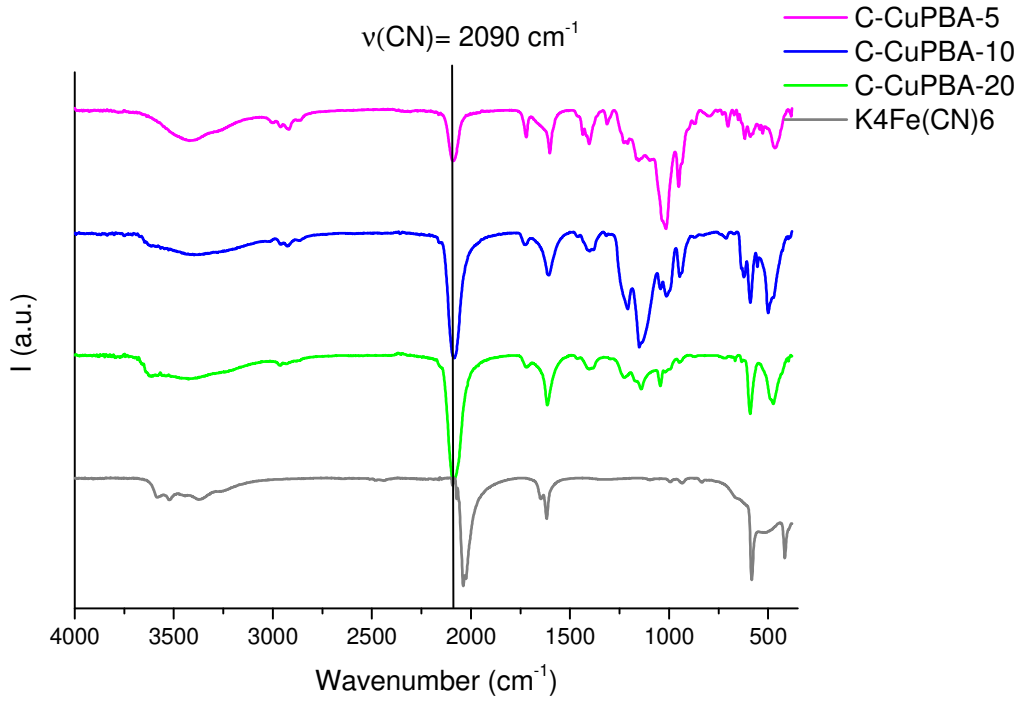

In the entire spectrum, the bands related to water are observed. The stretching vibrations of the O-H bound are present around 3400 cm^{-1} and the bending vibration of H-O-H at 1616 cm^{-1}. Some signals related to hydration water molecules of potassium ions present in the lattice cages are also visible for w=10 and w=20 (see Figure S4). CuPBA, and more generally PBA, are known to present some vacancies in the lattice structure when synthesized in water[64,65]. When these crystal defects are numerous enough, FTIR peaks appear as broad bands centred around 3540cm^{-1} and 3610cm^{-1}. This is related with the presence of quite free hydration water molecules inside the lattice of CuPBA. Moreover, the overall vibrations related to the CuPBA are more intense when the w increases because the quantity of material increases too. Several peaks due to organic traces are more visible at low values of w, with at 1720 cm^{-1}, vibrations corresponding to the ester function in NaAOT molecule[66] at 1210 cm^{-1} the stretching vibration of C=O bound and at 1150 cm^{-1}, the stretching vibration of the C-O bound.

Moreover at 2986 and 2913 cm^{-1}, peaks related to the stretching vibrations of C-H and CH_3 bounds and the bending vibration of C-H at 1400 cm^{-1} from surfactant were also visible. Those peaks related to surfactant were more intense for sample with lower w because the mass ratio of surfactant to CuPBA is higher in these conditions.

Figure 8: XRD analysis of the samples C-CuPBA-w for different w.

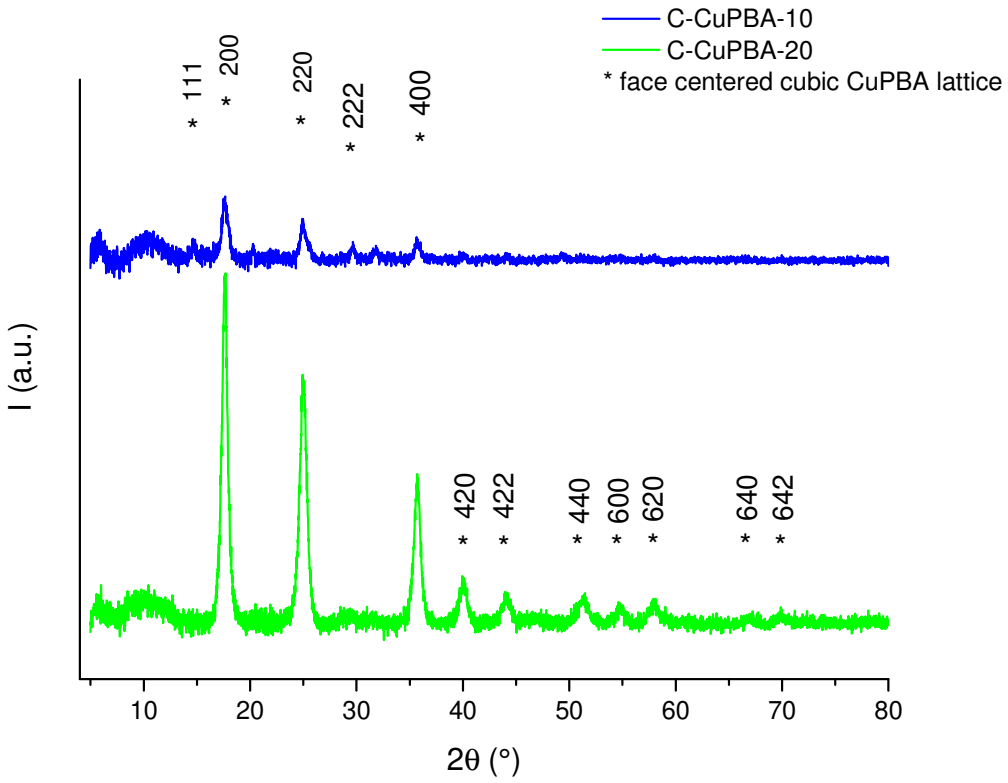

To confirm the synthesis of CuPBA NPs, XRD analyses were done (Figure 8). Sample C-CuPBA-5 is not presented because of the too small amount of material collected for this low value of w. For other samples, CuPBA characteristic diffraction peaks are observed as face centered cubic crystal lattice structure[23,63]. For w=10, the diffraction peaks intensity is quite weak. As general rule, when w increases, the quantity and crystallinity of material increases too and the diffractograms are more precise.

Therefore, FTIR and XRD results allowed to conclude that CuPBA NPs were well synthesized as the face centered cubic crystal lattice structure.

Figure 9: TEM images for CuPBA NPs for different w (C-CuPBA-w).

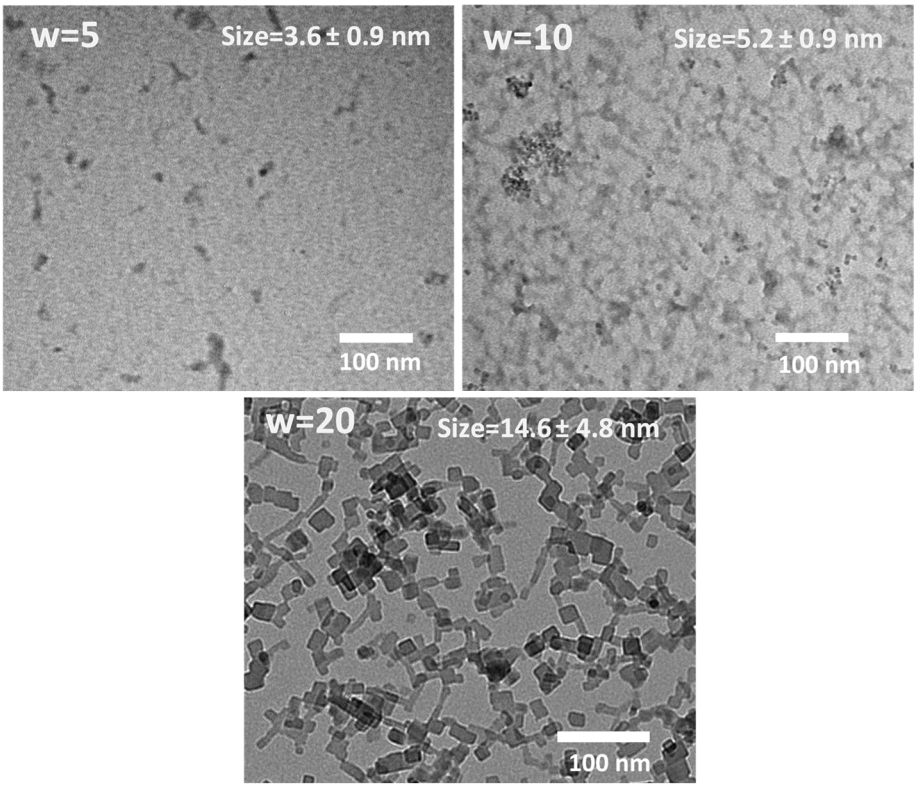

The morphology of the NPs was also studied. Figure 9 shows TEM images of CuPBA NPs synthesised using an inverse microemulsion with different w. The average sizes are shown and the size distributions for each system are also given in ESI (Fig. S5). It is clear that no superlattices are observed confirming the findings of Mann and Moulik[27,29]. Apart from the fact that the CuPBA system is not favourable for the observation of superstructures, the synthesis time was much shorter in our case and could also explain this result.

In the TEM image of the C-CuPBA-5 sample, very small NPs are observed. For this low w=5, the droplets are very small and it is very difficult to distinguish NPs from aggregates. These aggregates are probably formed after the break-up of the microemulsion, due to the drying of the droplet deposited on the TEM grid surface. As no diffractograms can be extracted from this system and TEM observations are difficult, the shape of these NPs remains uncertain. They could be square-shaped but also the first seeds of the emerging CuPBA crystal lattice.

Thus, the observation of other samples with a higher w is preferable. The C-CuPBA-10 sample shows an entanglement of nanoparticles with an average size of 5.2nm. In this tangle, the NPs could be interconnected by surfactant residues. This result is of the same order of magnitude as the particles measured by SANS (7.6 nm, considering the Guinier radius of 3.8nm in Figure 6).

The C-CuPBA-20 sample showed a significant amount of interconnected cubic nanoparticles. The average size is given as 14.2nm for this sample, but with a fairly wide size distribution.

Figure 10: Scale scheme of the micelles and CuPBA NPs obtained with regard to w values

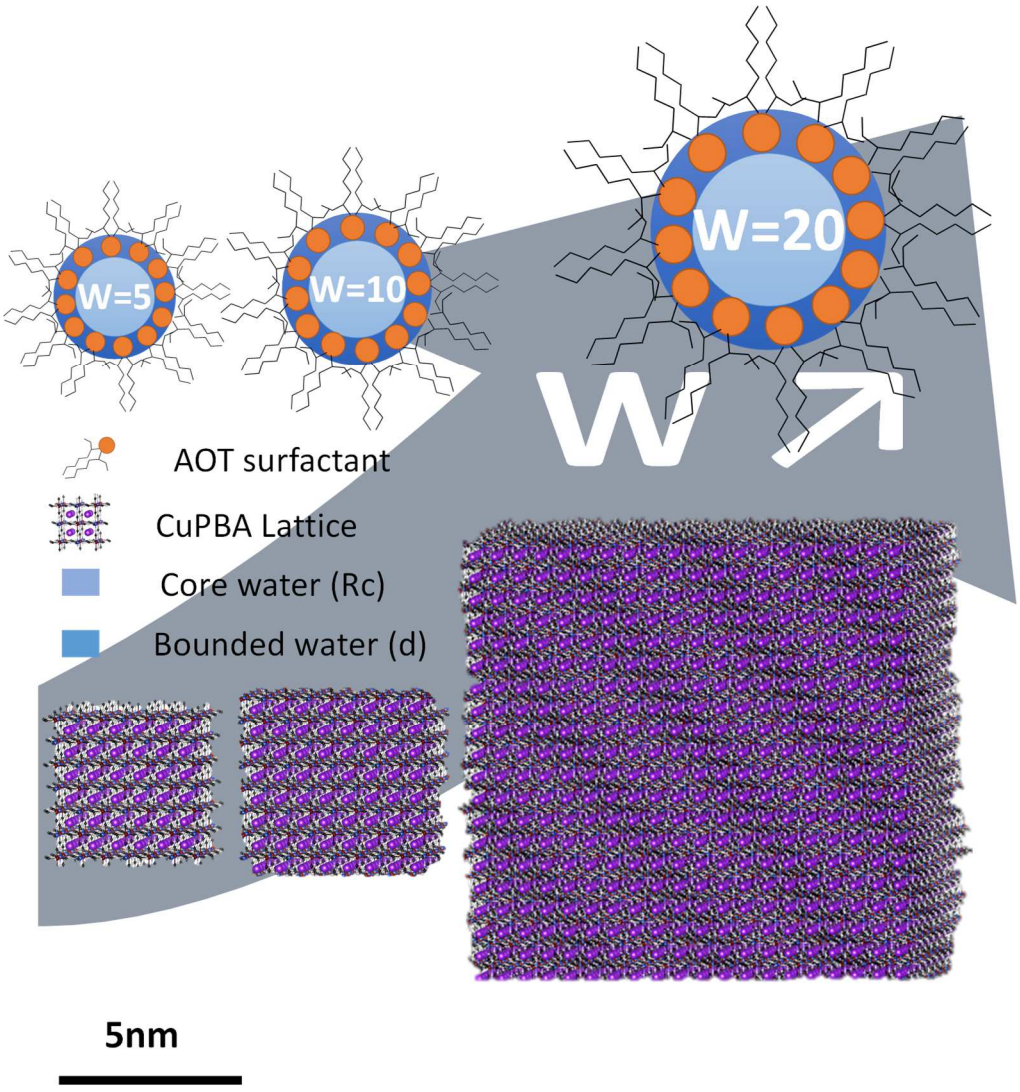

Figure 10 summarises the characteristic sizes obtained either by diffusion techniques (Rc, d) or by TEM (average sizes of CuPBA NPs). This diagram is drawn with respect to the scale of each parameter. Rc and d are taken from Table 3 while the average sizes of the crystal lattices forming the CuPBA NPs are taken from Figure 9. It is clear that for low values of w, the size of the CuPBA NPs corresponds to the size of the reverse micelles. The CuPBA NPs precipitate not only in the bulk water but also in the bound water region representing the micelle shell. This means that precipitation also occurs between the polar heads of the surfactants. This may alter the micelles slightly and could explain why long-range interactions are observed in the SAXS curves in Figure 4. For a high w as in the case of w=20, the system is close to instability leading to a sudden increase in the size of the NPs with a much wider distribution (Figure S4). The NPs are thus larger than the reverse micelles in which CuPBA precipitation occurs. However, there is still a template effect that keeps the size of the NPs quite low and prevents the precipitation of micron-sized particles.

In conclusion, the morphological and chemical analyses indicate that the particles formed are clearly CuPBA. Moreover, in contrast to the classical synthesis, very small CuPBA nanoparticles can be prepared via an inverse microemulsion.

4 CONCLUSIONS

The synthesis of CuPBA is possible using reverse microemulsions. In contrast to conventional aqueous routes, reverse microemulsions allow the synthesis of CuPBA particles of nanometric size. It is important to note that the microemulsions used to produce CuPBA NPs, whether prepared with NaAOT or with a modified CuAOT surfactant, did not show sedimented particles even after several days, implying reproducible synthesis routes. X-ray scattering techniques were found to be very relevant for characterising the microemulsions at the time of NP formation. SAXS data revealed that long-range interactions between droplets appear even

for systems containing small amounts of water and solute, i.e. for small values of w. These interactions are only visible when CuPBA NPs are present in the droplets and could be related to the superlattice organisation of the NPs observed by Mann in the literature. While SAXS provided information on droplet size and interactions through the electron contrast between water and isooctane, the SANS technique allowed the study of CuPBA NPs during their formation inside the water droplets. By considering the adequate contrast by adjusting the D/H ratios in the organic and aqueous phases, it was possible to evaluate the size of CuPBA NPs in water droplets. It was found that the size of the NPs was very close to that determined by TEM, i.e. less than 10 nm. Chemical analyses (FTIR and XRD) were additional clues to prove the synthesis of CuPBA NPs through reverse microemulsions.

References

[1] G. Maurin-Pasturel, J. Long, M.A. Palacios, C. Guérin, C. Charnay, M.-G. Willinger, A.A. Trifonov, J. Larionova, Y. Guari, Engineered Au Core@Prussian Blue Analogous Shell Nanoheterostructures: Their Magnetic and Optical Properties, Chem. – Eur. J. 23 (2017) 7483–7496. https://doi.org/10.1002/chem.201605903.

[2] Y. Morioka, T. Hisamitsu, H. Inoue, N. Yoshioka, H. Tomizawa, E. Miki, Light-Induced Mixed-Valence State of FeII[Fe(CN)5NO]·xH2O, Bull. Chem. Soc. Jpn. 71 (1998) 837–844. https://doi.org/10.1246/bcsj.71.837.

[3] P. Franz, C. Ambrus, A. Hauser, D. Chernyshov, M. Hostettler, J. Hauser, L. Keller, K. Krämer, H. Stoeckli-Evans, P. Pattison, H.-B. Bürgi, S. Decurtins, Crystalline, Mixed-Valence Manganese Analogue of Prussian Blue: Magnetic, Spectroscopic, X-ray and Neutron Diffraction Studies, J. Am. Chem. Soc. 126 (2004) 16472–16477. https://doi.org/10.1021/ja0465451.

[4] M.N. Chong, B. Jin, C.W.K. Chow, C. Saint, Recent developments in photocatalytic water treatment technology: A review, Water Res. 44 (2010) 2997–3027. https://doi.org/10.1016/j.watres.2010.02.039.

[5] L. Jiang, X.-L. Feng, T.-B. Lu, S. Gao, Synthesis, Structures, and Magnetic Properties of a Series of Cyano-Bridged Fe−Mn Bimetallic Complexes, Inorg. Chem. 45 (2006) 5018–5026. https://doi.org/10.1021/ic052168x.

[6] M.P. Shores, J.J. Sokol, J.R. Long, Nickel(II)−Molybdenum(III)−Cyanide Clusters: Synthesis and Magnetic Behavior of Species Incorporating [(Me3tacn)Mo(CN)3], J. Am. Chem. Soc. 124 (2002) 2279–2292. https://doi.org/10.1021/ja011645h.

[7] A. Kumar, A.B. Kanagare, S. Banerjee, P. Kumar, M. Kumar, Jagannath, V. Sudarsan, Synthesis of cobalt hexacyanoferrate nanoparticles and its hydrogen storage properties, Int. J. Hydrog. Energy. 43 (2018) 7998–8006. https://doi.org/10.1016/j.ijhydene.2018.03.011.

[8] C.-P. Zhang, P. Gu, J. Zhao, D. Zhang, Y. Deng, Research on the treatment of liquid waste containing cesium by an adsorption–microfiltration process with potassium zinc hexacyanoferrate, J. Hazard. Mater. 167 (2009) 1057–1062. https://doi.org/10.1016/j.jhazmat.2009.01.104.

[9] T.P. Valsala, S.C. Roy, J.G.Shah, J. Gabriel, K. Raj, V. Venugopal, Removal of radioactive caesium from low level radioactive waste (LLW) streams using cobalt ferrocyanide impregnated organic anion exchanger, J. Hazard. Mater. 166 (2009) 1148–1153. https://doi.org/10.1016/j.jhazmat.2008.12.019.

[10] D. Parajuli, A. Kitajima, A. Takahashi, H. Tanaka, H. Ogawa, Y. Hakuta, K. Yoshino, T. Funahashi, M. Yamaguchi, M. Osada, T. Kawamoto, Application of Prussian blue nanoparticles for the radioactive Cs decontamination in Fukushima region, J. Environ. Radioact. 151 (2016) 233–237. https://doi.org/10.1016/j.jenvrad.2015.10.014.

[11] L. Zhang, L. Chen, X. Zhou, Z. Liu, Towards High-Voltage Aqueous Metal-Ion Batteries Beyond 1.5 V: The Zinc/Zinc Hexacyanoferrate System, Adv. Energy Mater. 5 (2015) 1400930. https://doi.org/10.1002/aenm.201400930.

[12] C.D. Wessells, S.V. Peddada, R.A. Huggins, Y. Cui, Nickel Hexacyanoferrate Nanoparticle Electrodes For Aqueous Sodium and Potassium Ion Batteries, Nano Lett. 11 (2011) 5421–5425. https://doi.org/10.1021/nl203193q.

[13] C.D. Wessells, R.A. Huggins, Y. Cui, Copper hexacyanoferrate battery electrodes with long cycle life and high power, Nat. Commun. 2 (2011) 550. https://doi.org/10.1038/ncomms1563.

[14] L. Wang, J. Song, R. Qiao, L.A. Wray, M.A. Hossain, Y.-D. Chuang, W. Yang, Y. Lu, D. Evans, J.-J. Lee, S. Vail, X. Zhao, M. Nishijima, S. Kakimoto, J.B. Goodenough, Rhombohedral Prussian White as Cathode for Rechargeable Sodium-Ion Batteries, J. Am. Chem. Soc. 137 (2015) 2548–2554. https://doi.org/10.1021/ja510347s.

[15] L. Wang, Y. Lu, J. Liu, M. Xu, J. Cheng, D. Zhang, J.B. Goodenough, A Superior Low-Cost Cathode for a Na-Ion Battery, Angew. Chem. Int. Ed. 52 (2013) 1964–1967. https://doi.org/10.1002/anie.201206854.
[16] C.D. Wessells, M.T. McDowell, S.V. Peddada, M. Pasta, R.A. Huggins, Y. Cui, Tunable Reaction Potentials in Open Framework Nanoparticle Battery Electrodes for Grid-Scale Energy Storage, ACS Nano. 6 (2012) 1688–1694. https://doi.org/10.1021/nn204666v.
[17] A.L. Lipson, S.-D. Han, S. Kim, B. Pan, N. Sa, C. Liao, T.T. Fister, A.K. Burrell, J.T. Vaughey, B.J. Ingram, Nickel hexacyanoferrate, a versatile intercalation host for divalent ions from nonaqueous electrolytes, J. Power Sources. 325 (2016) 646–652. https://doi.org/10.1016/j.jpowsour.2016.06.019.
[18] R. Trócoli, G. Kasiri, F. La Mantia, Phase transformation of copper hexacyanoferrate (KCuFe(CN)6) during zinc insertion: Effect of co-ion intercalation, J. Power Sources. 400 (2018) 167–171. https://doi.org/10.1016/j.jpowsour.2018.08.015.
[19] Y. Qing, J. Li, B. Kang, S. Chang, Y. Dai, Q. Long, C. Yuan, Selective sorption mechanism of Cs+ on potassium nickel hexacyanoferrate(II) compounds, J. Radioanal. Nucl. Chem. 304 (2015) 527–533. https://doi.org/10.1007/s10967-014-3876-5.
[20] S. Kawamura, S. Shibata, K. Kurotaki, H. Takeshita, The sorption characteristics of radionuclides on copper hexacyanoferrate(II), and the determination of 137cs in sea water, Anal. Chim. Acta. 102 (1978) 225–228. https://doi.org/10.1016/S0003-2670(01)93481-6.
[21] C. Loos-Neskovic, S. Ayrault, V. Badillo, B. Jimenez, E. Garnier, M. Fedoroff, D.J. Jones, B. Merinov, Structure of copper-potassium hexacyanoferrate (II) and sorption mechanisms of cesium, J. Solid State Chem. 177 (2004) 1817–1828. https://doi.org/10.1016/j.jssc.2004.01.018.
[22] J. Causse, A. Tokarev, J. Ravaux, M. Moloney, Y. Barré, A. Grandjean, Facile one-pot synthesis of copper hexacyanoferrate nanoparticle functionalised silica monoliths for the selective entrapment of 137Cs, J. Mater. Chem. A. 2 (2014) 9461–9464. https://doi.org/10.1039/C4TA01266F.
[23] A. Sommer-Marquez, C. Mansas, N. Talha, C. Rey, J. Causse, Reinforced silica monoliths functionalised with metal hexacyanoferrates for cesium decontamination: a combination of a one-pot procedure and skeleton calcination, RSC Adv. 6 (2016) 73475–73484. https://doi.org/10.1039/C6RA16980E.
[24] C. Delchet, A. Tokarev, X. Dumail, G. Toquer, Y. Barré, Y. Guari, C. Guerin, J. Larionova, A. Grandjean, Extraction of radioactive cesium using innovative functionalized porous materials, RSC Adv. 2 (2012) 5707–5716. https://doi.org/10.1039/C2RA00012A.
[25] S. Ayrault, B. Jimenez, E. Garnier, M. Fedoroff, D.J. Jones, C. Loos-Neskovic, Sorption Mechanisms of Cesium on CuII2FeII(CN)6and CuII3[FeIII(CN)6]2Hexacyanoferrates and Their Relation to the Crystalline Structure, J. Solid State Chem. 141 (1998) 475–485. https://doi.org/10.1006/jssc.1998.7997.
[26] Z. Jia, B. Wang, Y. Wang, Copper hexacyanoferrate with a well-defined open framework as a positive electrode for aqueous zinc ion batteries, Mater. Chem. Phys. 149–150 (2015) 601–606. https://doi.org/10.1016/j.matchemphys.2014.11.014.
[27] S. Vaucher, M. Li, S. Mann, Synthesis of Prussian Blue Nanoparticles and Nanocrystal Superlattices in Reverse Microemulsions, Angew. Chem. Int. Ed. 39 (2000) 1793–1796. https://doi.org/10.1002/(SICI)1521-3773(20000515)39:10<1793::AID-ANIE1793>3.0.CO;2-Y.
[28] S. Vaucher, J. Fielden, M. Li, E. Dujardin, S. Mann, Molecule-Based Magnetic Nanoparticles: Synthesis of Cobalt Hexacyanoferrate, Cobalt Pentacyanonitrosylferrate, and Chromium Hexacyanochromate Coordination Polymers in Water-in-Oil Microemulsions, Nano Lett. 2 (2002) 225–229. https://doi.org/10.1021/nl0156538.
[29] S.P. Moulik, G.C. De, A.K. Panda, B.B. Bhowmik, A.R. Das, Dispersed Molecular Aggregates. 1. Synthesis and Characterization of Nanoparticles of Cu2[Fe(CN)6] in H2O/AOT/n-Heptane Water-in-Oil Microemulsion Media, Langmuir. 15 (1999) 8361–8367. https://doi.org/10.1021/la9813533.

[30] M.F. Dumont, O.N. Risset, E.S. Knowles, T. Yamamoto, D.M. Pajerowski, M.W. Meisel, D.R. Talham, Synthesis and Size Control of Iron(II) Hexacyanochromate(III) Nanoparticles and the Effect of Particle Size on Linkage Isomerism, Inorg. Chem. 52 (2013) 4494–4501. https://doi.org/10.1021/ic302764k.
[31] Z. Li, J. Zhang, T. Mu, J. Du, Z. Liu, B. Han, J. Chen, Preparation of polyvinylpyrrolidone-protected Prussian blue nanocomposites in microemulsion, Colloids Surf. Physicochem. Eng. Asp. 243 (2004) 63–66. https://doi.org/10.1016/j.colsurfa.2004.05.010.
[32] A. Gutiérrez-Becerra, M. Barcena-Soto, V. Soto, J. Arellano-Ceja, N. Casillas, S. Prévost, L. Noirez, M. Gradzielski, J.I. Escalante, Structure of reverse microemulsion-templated metal hexacyanoferrate nanoparticles, Nanoscale Res. Lett. 7 (2012) 83. https://doi.org/10.1186/1556-276X-7-83.
[33] M.A. Malik, M.Y. Wani, M.A. Hashim, Microemulsion method: A novel route to synthesize organic and inorganic nanomaterials: 1st Nano Update, Arab. J. Chem. 5 (2012) 397–417. https://doi.org/10.1016/j.arabjc.2010.09.027.
[34] E. Nourafkan, H. Gao, Z. Hu, D. Wen, Formulation optimization of reverse microemulsions using design of experiments for nanoparticles synthesis, Chem. Eng. Res. Des. 125 (2017) 367–384. https://doi.org/10.1016/j.cherd.2017.07.023.
[35] A. Bumajdad, J. Eastoe, M.I. Zaki, R.K. Heenan, L. Pasupulety, Generation of metal oxide nanoparticles in optimised microemulsions, Mem. Profr. Hironobu Kunieda. 312 (2007) 68–75. https://doi.org/10.1016/j.jcis.2006.09.007.
[36] M.-P. Pileni, T. Zemb, C. Petit, Solubilization by reverse micelles: Solute localization and structure perturbation, Chem. Phys. Lett. 118 (1985) 414–420. https://doi.org/10.1016/0009-2614(85)85402-6.
[37] M. Hirai, R. Kawai-Hirai, M. Sanada, H. Iwase, S. Mitsuya, Characteristics of AOT Microemulsion Structure Depending on Apolar Solvents, J. Phys. Chem. B. 103 (1999) 9658–9662. https://doi.org/10.1021/jp991899d.
[38] L. Arleth, J.S. Pedersen, Droplet polydispersity and shape fluctuations in AOT [bis(2-ethylhexyl)sulfosuccinate sodium salt] microemulsions studied by contrast variation small-angle neutron scattering, Phys. Rev. E. 63 (2001) 061406.
[39] J.S. Pedersen, Analysis of small-angle scattering data from micelles and microemulsions: free-form approaches and model fitting, Curr. Opin. Colloid Interface Sci. 4 (1999) 190–196. https://doi.org/10.1016/S1359-0294(99)00033-3.
[40] D. Chatenay, W. Urbach, A.M. Cazabat, D. Langevin, Onset of Droplet Aggregation from Self-Diffusion Measurements in Microemulsions, Phys. Rev. Lett. 54 (1985) 2253–2256. https://doi.org/10.1103/PhysRevLett.54.2253.
[41] M.F. Khan, M.K. Singh, S. Sen, Measuring Size, Size Distribution, and Polydispersity of Water-in-Oil Microemulsion Droplets using Fluorescence Correlation Spectroscopy: Comparison to Dynamic Light Scattering, J. Phys. Chem. B. 120 (2016) 1008–1020. https://doi.org/10.1021/acs.jpcb.5b09920.
[42] A. Dukhin, P. Goetz, Evolution of water-in-oil emulsion controlled by droplet-bulk ion exchange: acoustic, electroacoustic, conductivity and image analysis, Colloids Surf. Physicochem. Eng. Asp. 253 (2005) 51–64. https://doi.org/10.1016/j.colsurfa.2004.10.125.
[43] M.P. Pileni, Mesostructured Fluids in Oil-Rich Regions: Structural and Templating Approaches, Langmuir. 17 (2001) 7476–7486. https://doi.org/10.1021/la010538y.
[44] M.P. Pileni, Reverse micelles as microreactors, J. Phys. Chem. 97 (1993) 6961–6973. https://doi.org/10.1021/j100129a008.
[45] S. Abel, Micelles inverses d'AOT et de C12E4: Structure et évaluation de leurs compressibilités par simulation de dynamique moléculaire, Université Pierre et Marie Curie- Paris V, 2007.
[46] M.P. Pileni, I. Lisiecki, Nanometer metallic copper particle synthesis in reverse micelles, Colloids Surf. Physicochem. Eng. Asp. 80 (1993) 63–68. https://doi.org/10.1016/0927-7757(93)80224-3.

[47] J.P. Chen, K.M. Lee, C.M. Sorensen, K.J. Klabunde, G.C. Hadjipanayis, Magnetic properties of microemulsion synthesized cobalt fine particles, J. Appl. Phys. 75 (1994) 5876–5878. https://doi.org/10.1063/1.355546.
[48] M. Chen, Y. Wu, S. Zhou, L. Wu, Shape-Controllable Synthesis of Crystalline Ni Complex Particles via AOT-based Microemulsions, J. Phys. Chem. B. 112 (2008) 6536–6541. https://doi.org/10.1021/jp711932h.
[49] J. Esquena, Th.F. Tadros, K. Kostarelos, C. Solans, Preparation of Narrow Size Distribution Silica Particles Using Microemulsions, Langmuir. 13 (1997) 6400–6406. https://doi.org/10.1021/la9705120.
[50] J.A. López Pérez, M.A. López Quintela, J. Mira, J. Rivas, S.W. Charles, Advances in the Preparation of Magnetic Nanoparticles by the Microemulsion Method, J. Phys. Chem. B. 101 (1997) 8045–8047. https://doi.org/10.1021/jp972046t.
[51] V.F. Kamalov, R. Little, S.L. Logunov, M.A. El-Sayed, Picosecond Electronic Relaxation in CdS/HgS/CdS Quantum Dot Quantum Well Semiconductor Nanoparticles, J. Phys. Chem. 100 (1996) 6381–6384. https://doi.org/10.1021/jp953708m.
[52] W.C.W. Chan, D.J. Maxwell, X. Gao, R.E. Bailey, M. Han, S. Nie, Luminescent quantum dots for multiplexed biological detection and imaging, Curr. Opin. Biotechnol. 13 (2002) 40–46. https://doi.org/10.1016/S0958-1669(02)00282-3.
[53] M.A. López-Quintela, Synthesis of nanomaterials in microemulsions: formation mechanisms and growth control, Curr. Opin. Colloid Interface Sci. 8 (2003) 137–144. https://doi.org/10.1016/S1359-0294(03)00019-0.
[54] L. Catala, D. Brinzei, Y. Prado, A. Gloter, O. Stéphan, G. Rogez, T. Mallah, Core–Multishell Magnetic Coordination Nanoparticles: Toward Multifunctionality on the Nanoscale, Angew. Chem. Int. Ed. 48 (2009) 183–187. https://doi.org/10.1002/anie.200804238.
[55] J. Wang, Z.H. Shah, S. Zhang, R. Lu, Silica-based nanocomposites via reverse microemulsions: classifications, preparations, and applications, Nanoscale. 6 (2014) 4418–4437. https://doi.org/10.1039/C3NR06025J.
[56] I. Lisiecki, F. Billoudet, M.P. Pileni, Syntheses of copper nanoparticles in gelified microemulsion and in reverse micelles, Organised Assem. Surfactants Solut. 72 (1997) 251–261. https://doi.org/10.1016/S0167-7322(97)00041-X.
[57] C.J. Johnson, M. Li, S. Mann, Seed-Assisted Synthesis of BaCrO4 Nanoparticles and Nanostructures in Water-in-Oil Microemulsions, Adv. Funct. Mater. 14 (2004) 1233–1239. https://doi.org/10.1002/adfm.200400197.
[58] J. Eastoe, G. Fragneto, B.H. Robinson, T.F. Towey, R.K. Heenan, F.J. Leng, Variation of surfactant counterion and its effect on the structure and properties of Aerosol-OT-based water-in-oil microemulsions, J. Chem. Soc. Faraday Trans. 88 (1992) 461–471. https://doi.org/10.1039/FT9928800461.
[59] M. Kotlarchyk, J.S. Huang, S.H. Chen, Structure of AOT reversed micelles determined by small-angle neutron scattering, J. Phys. Chem. 89 (1985) 4382–4386. https://doi.org/10.1021/j100266a046.
[60] M. Maugey, A.-M. Bellocq, Effect of Added Salt and Poly(ethylene glycol) on the Phase Behavior of a Balanced AOT−Water−Oil System, Langmuir. 15 (1999) 8602–8608. https://doi.org/10.1021/la990438g.
[61] Y.M. Harshe, L. Ehrl, M. Lattuada, Hydrodynamic properties of rigid fractal aggregates of arbitrary morphology, J. Colloid Interface Sci. 352 (2010) 87–98. https://doi.org/10.1016/j.jcis.2010.08.040.
[62] R. Fortes Martín, C. Prietzel, J. Koetz, Template-mediated self-assembly of magnetite-gold nanoparticle superstructures at the water-oil interface of AOT reverse microemulsions, J. Colloid Interface Sci. 581 (2021) 44–55. https://doi.org/10.1016/j.jcis.2020.07.079.
[63] A. Grandjean, C. Delchet, J. Causse, Y. Barré, Y. Guari, J. Larionova, Effect of the chemical nature of different transition metal ferrocyanides to entrap Cs, J. Radioanal. Nucl. Chem. 307 (2016) 427–436. https://doi.org/10.1007/s10967-015-4098-1.

[64] A. Azhar, Y. Li, Z. Cai, M.B. Zakaria, M.K. Masud, Md.S.A. Hossain, J. Kim, W. Zhang, J. Na, Y. Yamauchi, M. Hu, Nanoarchitectonics: A New Materials Horizon for Prussian Blue and Its Analogues, Bull. Chem. Soc. Jpn. 92 (2019) 875–904. https://doi.org/10.1246/bcsj.20180368.
[65] W. Li, C. Han, G. Cheng, S. Chou, H. Liu, S. Dou, Chemical Properties, Structural Properties, and Energy Storage Applications of Prussian Blue Analogues, Small. 15 (2019) 1900470. https://doi.org/10.1002/smll.201900470.
[66] G. Calvaruso, A. Minore, V.T. Liveri, FT-IR Investigation of the Urea State in AOT Reversed Micelles, J. Colloid Interface Sci. 243 (2001) 227–232. https://doi.org/10.1006/jcis.2001.7878.

Table 3

Samples	w	Form Factor				Contrast		Structure Factor	
		N (ob/cm^3)	R (nm)	d (nm)	R_{tot} (nm)	$\Delta\rho_1$ (cm^{-2})	$\Delta\rho_2$ (cm^{-2})	R_{agg} (nm)	D
C-H_2O-5	5	$2.25\ 10^{18}$	0.9	0.8	1.7	$3.04\ 10^{10}$	$4.39\ 10^{10}$		
C-H_2O-10	10	$8.04\ 10^{17}$	1.3	0.9	2.2	$3.04\ 10^{10}$	$4.39\ 10^{10}$		
C-H_2O-20	20	$2.40\ 10^{17}$	2.2	1.2	3.4	$3.04\ 10^{10}$	$4.39\ 10^{10}$		
C-CuPBA-5	5	$2.25\ 10^{18}$	0.9	0.8	1.7	$3.04\ 10^{10}$	$4.39\ 10^{10}$	30.4	1.9
C-CuPBA-10	10	$8.97\ 10^{17}$	1.3	0.9	2.2	$3.04\ 10^{10}$	$4.39\ 10^{10}$	20.0	2.0
C-CuPBA-20	20	$2.73\ 10^{17}$	2.2	0.9	3.1	$3.04\ 10^{10}$	$4.39\ 10^{10}$	21.0	2.2

Table S1

	Samples	w	Form Factor				Contrast		Structure Factor	
			N (ob/cm^3)	R (nm)	d (nm)	R_{tot} (nm)	$\Delta\rho_1$ (cm^{-2})	$\Delta\rho_2$ (cm^{-2})	R_{agg} (nm)	D
Fig. S1	A-H_2O-5	5.6	$2.90\ 10^{18}$	0.7	0.8	1.5	$3.04\ 10^{10}$	$4.39\ 10^{10}$		
	A-H_2O-11	11.1	$9.32\ 10^{17}$	1.2	0.8	2.0	$3.04\ 10^{10}$	$4.39\ 10^{10}$		
	A-H_2O-22	22.3	$1.91\ 10^{17}$	2.6	1.0	3.6	$3.04\ 10^{10}$	$4.39\ 10^{10}$		
Fig. S2	A-H_2O-5	5	$1.71\ 10^{18}$	0.8	0.8	1.6	$3.04\ 10^{10}$	$4.39\ 10^{10}$		
	B-H_2O-5	5	$3.93\ 10^{18}$	0.5	0.8	1.3	$3.04\ 10^{10}$	$4.39\ 10^{10}$		
	C-H_2O-5	5	$9.12\ 10^{18}$	0.4	0.7	1.1	$3.04\ 10^{10}$	$4.39\ 10^{10}$		
Fig. S3	A-Fe-5	5	$7.33\ 10^{18}$	0.5	0.6	1.1	$3.04\ 10^{10}$	$4.39\ 10^{10}$		
	A-Fe-10	10	$5.57\ 10^{18}$	0.7	0.9	1.6	$3.04\ 10^{10}$	$4.39\ 10^{10}$		
	A-H_2O-5	5	$1.71\ 10^{18}$	0.8	0.8	1.6	$3.04\ 10^{10}$	$4.39\ 10^{10}$		
	A-H_2O-10	10	$7.2\ 10^{18}$	1.4	0.8	2.2	$3.04\ 10^{10}$	$4.39\ 10^{10}$		
Fig. S4	A-Fe-5	5	$7.33\ 10^{18}$	0.5	0.6	1.1	$3.04\ 10^{10}$	$4.39\ 10^{10}$		
	B-H_2O-5	5	$3.93\ 10^{18}$	0.5	0.8	1.3	$3.04\ 10^{10}$	$4.39\ 10^{10}$		
	C-CuPBA-5	5	$2.25\ 10^{18}$	0.9	0.8	1.7	$3.04\ 10^{10}$	$4.39\ 10^{10}$	30.4	1.88

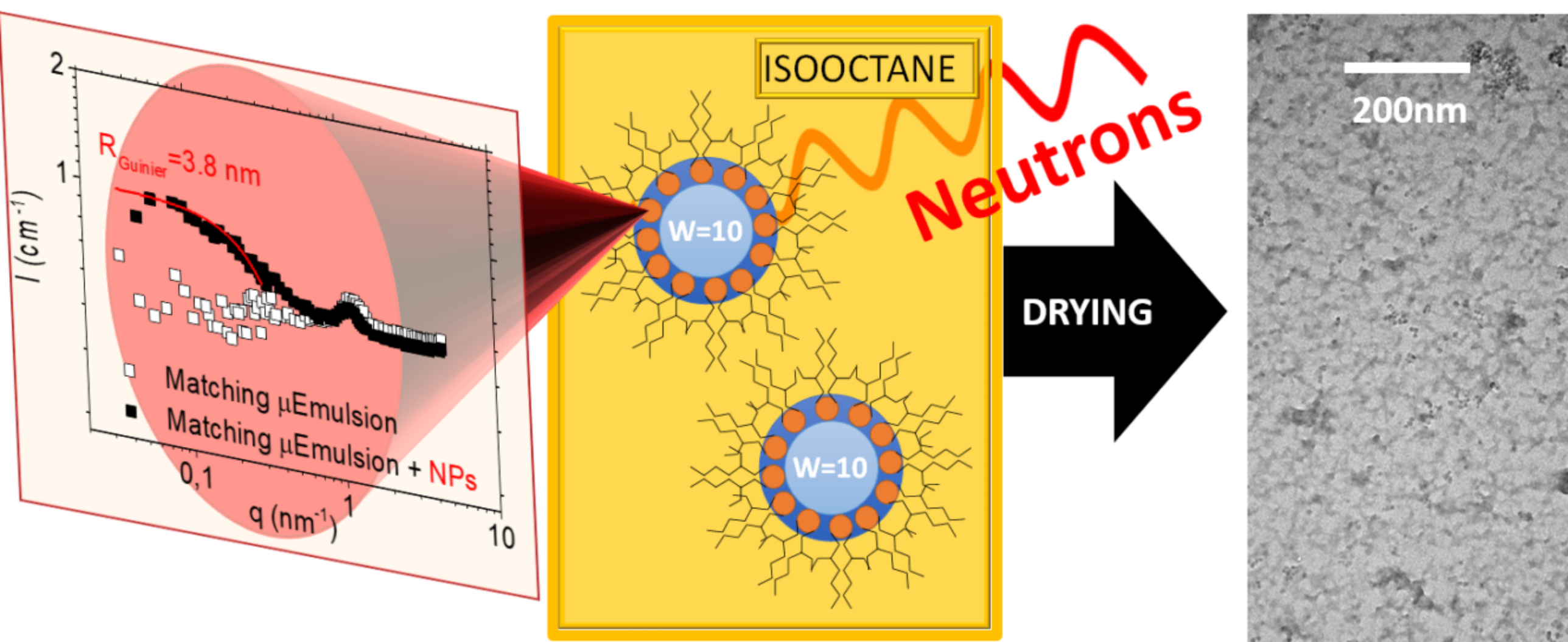
2
1
I (cm-1)
RGuinier=3.8 nm
Matching µEmulsion
Matching µEmulsion + NPs
0,1
q (nm-1)
1
10
ISOOCTANE
W=10
W=10
Neutrons
DRYING
200nm